Model Characterization of Magnetic Microrobot Navigating in Viscous Environment

Karim Belharet[1], Chunbo Yang[2], David Folio[3], and Antoine Ferreira[3]

[1] Laboratoire PRISME, Hautes Études d'Ingénieur campus Centre,
Site Balsan, 2 allée Jean Vaillé, 36000 Châteauroux.
[2] Tongji University, 4800 Cao'an road, Shangai, P.R. China.
[3] École Nationale Supérieure d'Ingénieurs de Bourges, Univ. Orléans, Laboratoire PRISME,
88 bld Lahitolle, F-18020 Bourges, France,
david.folio@ensi-bourges.fr,antoine.ferreira@ensi-bourges.fr

Abstract. In this paper we aim to characterize and validate the system's dynamic model of a magnetic microrobot navigating in viscous flow. First, the controlled magnetic forces exerted on the magnetic microrobot was calibrated, validating the magnetic model. Secondly, the external forces were characterized on-line from digital microscope measurements. Especially, unlike common approaches used with microscope where orthographic projection model were used, we have proposed to consider the weak-perspective model. Thus, the proposed vision-based force characterization allows us to retrieve the 3D translational velocities and accelerations of the magnetic microrobot viewed from a digital microscope. Experimental results in two different environments illustrate the efficiency of the proposed method.

1 Introduction

Untethered microrobots have the potential to dramatically change many aspects of medicine by navigating through bodily fluids to perform targeted diagnosis and therapy [1, 2]. The use of magnetic fields is till now the most used approach, and different designs have been proposed in the literature [2, 3]. One most advanced design relies on bead pulling since *in-vivo* experiments were conducted in the carotid artery of a living swine [4]. Thus, in this work we consider a spherical neodymium magnet as microrobot body (termed *microrobot* throughout the text). Nevertheless, all these contributions point out the problem of navigation controllability of magnetic microrobots in viscous flow when experimental endovascular applications are considered. Indeed most untethered microrobot propulsion schemes based on magnetic pulling have to face important constraints related to coils technology. To improve the magnetic navigation strategy against the biological laws governing patients body, a characterization of their behavior within microfluidic environments is mandatory.

Our motivation in this work is to characterize and validate the system's dynamic model of a magnetic microrobot navigating in viscous flow. Hence, we have first to validate the considered magnetic model, and calibrate the controlled magnetic forces exerted on the magnetic microrobot to ensure a reliable control scheme. Then, to understand the relationship between applied magnetization force and microrobot motion

in a fluidic environment, we have to characterize the interaction forces applied on the microrobot. Thus, this paper's main contribution is to define a mapping between the system dynamics and sensory data acquired from a digital microscope to characterize these interaction forces. Classically, when dealing with microscope the orthographic perspective model is considered, that is a scaling of the observed scene. However, pure orthographic projection is usually unrealistic, and methods that use orthographic projection are only valid in a limited domain where the distance and position effects can be neglected [5]. Therefore, we propose here to consider the weak-perspective model that is closer to the full perspective model, and allows to improve the knowledge of the external forces.

The paper is organized as follows. First, in Sect. 2 the controlled magnetic force is calibrated, and the magnetic model is validated. Sect. 3 briefly introduces the experimental setup that is used to operate magnetic microrobots in microfluidic environment, and the corresponding system's dynamic model. Sect. 4 is devoted to propose a mapping between the the vision-based model and the system's dynamic. Sect. 5 presents different experiments that illustrate the efficiency and robustness of the proposed framework. This paper is concluded in Sect. 6.

2 Magnetic Force Characterization

2.1 Controlled Magnetic Force

The efficiency of magnetic navigation strongly depends on the amount of magnetic driving force applied to the magnetic microrobot [6]. The knowledge of these steering magnetic forces is crucial for the design of reliable magnetic navigation control scheme. In this paper bead pulling of a hard-magnetic neodymium microsphere is considered. Hence, the magnetic forces $\mathbf{f}_\mathrm{m}$ generated by the magnetic gradients $\nabla\mathbf{b}$ on this magnetic microrobot, with hard magnetic material, could be formulated as [7]:

$$\mathbf{f}_\mathrm{m} = V_\mathrm{m}\mathbf{M}\nabla\mathbf{b} = K_\mathrm{m}\nabla\mathbf{b} \tag{1}$$

with V_m the magnetic volume of the ferromagnetic material, $\mathbf{M}$ the bead's magnetization, $\mathbf{b}$ the magnetic field and ∇ the gradient operator.

2.2 Magnetic Force Calibration

To calibrate the forces applied on the magnetic microrobot force measurements have been performed inside a known magnetic field using a FemtoTools FT-S270 capacitive force sensor. A 3-axis micromanipulator with integrated position encoders (SmarAct GmbH, SLC line) is used to move the sensor towards a permanent magnet. Hence, a neodymium microsphere is glued to the force sensor. During the displacement both the output signal of the force sensor and the position encoder is recorded. Fig. 1(a) shows the force sensor output signal wrt. the distance to the magnet of three NdFeB N35 microspheres with an approximately $250\,\mu\mathrm{m}$ radii. To ensure that magnetic forces are measured only, the measurement is repeated using the sensor without magnetic material attached to it. Since the magnetic forces acting upon magnetic material depend not

only on their intrinsic magnetic properties but also on both magnetic field intensity and gradient, accurate knowledge about the fields has to be obtained. The magnetic field strength along the position of the sample is then measured with a magnetometer (THM1176 Hall Magnetometer, Metrolab). Fig. 1(b) shows the field gradient that has been computed from the field strength measurement.

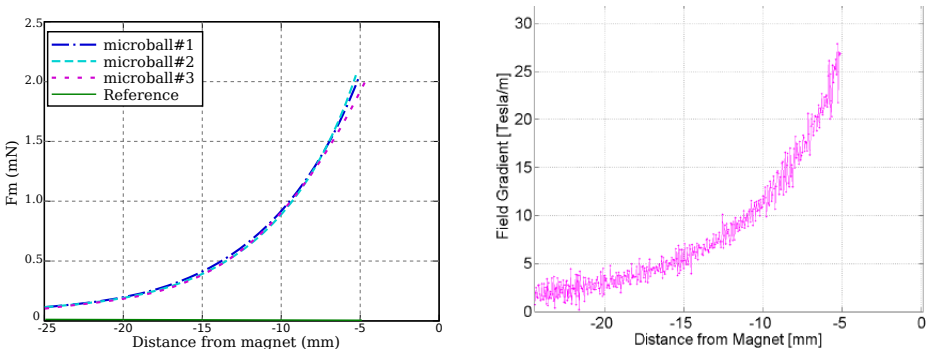

(a) (b)

Fig. 1. (a) Force measurement and (b) magnetic gradient strength on NdFeB N35 microsphere with an average radius $r = 250\,\mu\text{m}$

Finally, it can be shown that the field gradient $\nabla\mathbf{b}$ and force measurement shows a very similar curve shape. This allows us to validate the magnetic model (1), proposing a proportional relationship between force and field gradient: $\mathbf{f}_\text{m} \propto \nabla\mathbf{b}$, and then estimate the gain K_m values. Especially, for a NdFeB N35 microsphere with an approximately $V_\text{m} = 6.54 \times 10^{-11}\,\text{m}^3$ magnetic volume, and a magnetization of about $\mathbf{M} = 1.23 \times 10^6\,\text{A/m}$ [7], we get $K_\text{m} = 8.05 \times 10^{-5}\,\text{Am}^2$. This is consistent with observations depicted on Fig. 1(a) and 1(b).

3 Magnetic Microsphere Navigating In Microfluidic Environment

3.1 Electromagnetic Based Actuation Testbed

The motion control of our untethered microrobot in a microfluidic environment relies upon magnetic gradients $\nabla\mathbf{b}$. To this aim, an electromagnetic based actuation (EMA) testbed has been developed specifically by Aeon Scientific™ to generate the 3D controlled magnetic fields, and is illustrated in Fig. 2. The EMA setup consists of three nested sets of Maxwell coils and one nested set of Helmholtz coils, combined coaxially such that the magnetic field and magnetic gradient field can be controlled in the center of the workspace [1, 8, 9]. Table 1 shows the detailed characteristics of the EMA coils system. Such arrangement allows to generate homogeneous magnetic flux densities and uniform magnetic gradient field $\nabla\mathbf{b} = (\nabla b_x, \nabla b_y, \nabla b_z)^T$ relative to the

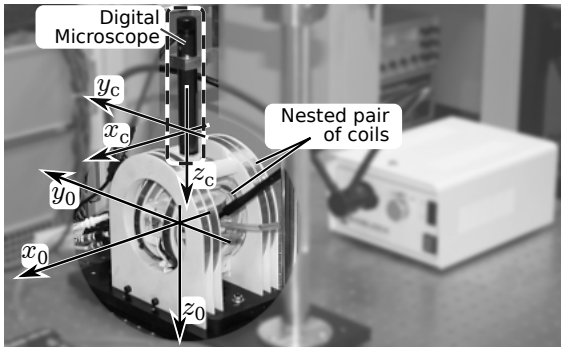

Fig. 2. Experimental testbed: EMA coils system and the digital microscope.

Table 1. Characteristic of the EMA system

Coils	Radius (mm)	Turns	Max. $\|\nabla\mathbf{b}\|$ (mT/m)	Max. $\|\mathbf{b}\|$ (mT)
∇b_x (outer)	72	80	208.67	–
∇b_y (middle)	51	58	301.53	–
∇b_z (inner)	34	45	526.38	–
$\mathbf{b}$ (field)	68	91	–	12.58

reference frame $\mathcal{F}_0$, in a workspace of $20\,\mathrm{mm} \times 20\,\mathrm{mm}$, as depicted on Fig. 3. Magnetic gradient forces will thus be exerted on the magnetic microrobot that is inside a microfluidic environment.

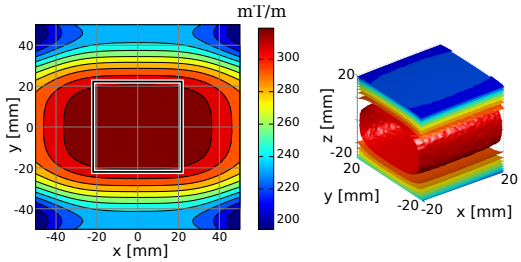

Fig. 3. Magnetic gradient field strength generated by the EMA coils inside the workspace.

Moreover, the magnetic setup is equipped with a CCD high-resolution miniature microscope camera (TIMM 400, Nanosensor) providing up to $26\,\mathrm{mm} \times 20\,\mathrm{mm}$ field of view. A robust tracking algorithm measure, with a sub-micrometer resolution, the location of the magnetic microrobot by real-time processing the video images acquired by the digital microscope.

3.2 Dynamic System Model

The considered microrobot body immersed in a microfluidic environment is modeled by a magnetic microsphere as illustrated on Fig. 4. The microrobot environment is modeled by a 3D Euclidean space, and we denote by $\mathcal{F}_0 = (O, \overrightarrow{x}_0, \overrightarrow{y}_0, \overrightarrow{z}_0)$ the absolute fixed frame, and $\mathcal{F}_c = (C, \overrightarrow{x}_c, \overrightarrow{y}_c, \overrightarrow{z}_c)$ the frame linked to the digital microscope, as shown on Fig. 2. Actuated by external magnetic gradients $\nabla \mathbf{b}$ in a microfluidic environment, the microrobot will mainly experience the controlled magnetic ($\mathbf{f}_\mathrm{m}$), apparent weight ($\mathbf{f}_g$), contact ($\mathbf{f}_\mathrm{c}$), electrostatic ($\mathbf{f}_\mathrm{e}$), van der Waals ($\mathbf{f}_\mathrm{v}$) and hydrodynamic drag ($\mathbf{f}_\mathrm{d}$) microforces that affect the microrobot's motion. The effects of these forces are explained in detail in [10]. Hence, the translational motion of the ferromagnetic microsphere is formulated as follow:

$$m\dot{\mathbf{v}} = \mathbf{f}_\mathrm{m} + \underbrace{\mathbf{f}_\mathrm{d} + \mathbf{f}_g + \mathbf{f}_\mathrm{v} + \mathbf{f}_\mathrm{e} + \mathbf{f}_\mathrm{c}}_{\mathbf{f}_\mathrm{Ex}} \tag{2}$$

where $\mathbf{v}$ is the translational velocity of the microrobot and m its mass.

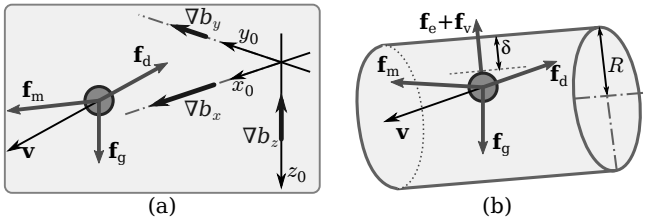

Fig. 4. Forces applied on microrobot navigating in microfluidic environment: (a) in an infinite extend and (b) in cylindric channel.

In the rest of this paper, we assume that: i) the orientation of the ferromagnetic microrobot does not change due to the magnetic torque which tends to align the magnetization of the robot along the magnetic field; ii) the ferromagnetic device is large enough to neglect the effect of Brownian motion; and iii) the microrobot is never in contact with the walls of the environment, namely $\mathbf{f}_\mathrm{c} = 0$.

4 Vision-Based External Forces Characterization

To get a more robust motion control strategy we aim to embed the interaction force $\mathbf{f}_\mathrm{Ex}$ defined in Eq. (2), leading to the need to characterize $\mathbf{f}_\mathrm{Ex}$ *on-line*. Therefore, we have to use sensors available on the previously presented EMA system's. As the sole sensor is a digital microscope, vision-based force characterization is used. Indeed, to characterize $\mathbf{f}_\mathrm{Ex}$, the mapping of system dynamic points to image pixels is required.

4.1 Projection Model

Classically, as illustrated in Fig. 5, a 3D point of coordinates $\mathbf{x} = (X, Y, Z)^T$ in the microscope frame $\mathcal{F}_c$ is projected into a 2D point with coordinates $\mathbf{s} = (x, y)^T$ in the image plane with a perspective projection, and yields:

$$x = \frac{X}{Z}, \qquad y = \frac{Y}{Z} \tag{3}$$

If we denote (u, v) the position of the corresponding pixel in the digitized image, this position is related to $\mathbf{s}$ by:

$$\begin{cases} u = u_0 + \alpha_u x \\ v = v_0 + \alpha_v y \end{cases} \tag{4}$$

where α_u and α_v are the ratio between the focal length and the size of a pixel, and $(u_0\, v_0)$ is the principal point coordinate in pixel (see Fig. 5). Then, these four parameters define the digital microscope intrinsic parameters, that is: $\boldsymbol{\xi}_{\text{in}} = \{\alpha_u\, \alpha_v\, u_0\, v_0\}$, and are calibrated off-line [11, 12].

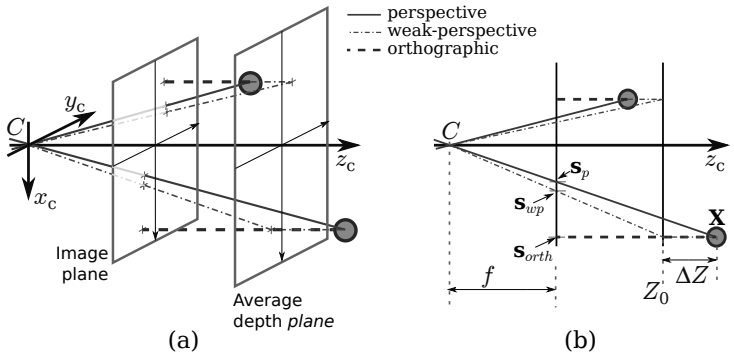

Fig. 5. Projection model: (a) 3D representation of image formation, and (b) full perspective ($\mathbf{s}_p$), weak-perspective ($\mathbf{s}_{wp}$) and orthographic perspective ($\mathbf{s}_{orth}$) projection models comparisons.

Generally, when a digital microscope is used, due to the sizes of the objects of interest wrt. the focal length f and the vision system distance, the orthographic projection model is considered, that is:

$$x = k_x X, \qquad y = k_y Y \tag{5}$$

where k_x and k_y scale the observed scene. As one can see, in orthographic projection, the depth Z of the point $\mathbf{x}$ does not affect its image formation. However, in neglecting the depth information, the orthographic projection models image formation incorrectly and solves for (approximately) known parameters as if they were unknowns. It is given the freedom to reconstruct wrong values for these artificial unknowns, which in turn can corrupt the recovery of the true unknowns. Therefore, methods that use orthographic

projection are only valid in a limited domain where the distance and position effects can be neglected.

Nevertheless, the full perspective projection model (3) requires a model or an estimation of the depth Z of the considered 3D point $\mathbf{x}$. Several approaches may be used to determine it. The most obvious solution is to measure it using dedicated sensors such as telemeters or stereoscopic systems. As our magnetic setup is not equipped with such sensors other approaches must be considered. For instance, it is possible to use structure from motion (SFM) techniques [13], signal processing methods [14], or even pose relative estimation [15]. Moreover, knowing an initial guess $Z(t_0)$, in [16] the authors propose to use the sensor/motion link to predict the Z-depth.

A much more suitable approximation is the weak-perspective projection, defined by:

$$x = \frac{X}{Z_0}, \qquad y = \frac{Y}{Z_0} \tag{6}$$

where Z_0 is an average depth plane, as shown on Fig. 5. The weak-perspective model is valid when the field of view is small and the average variation of the depth of the object (ΔZ) along the line of sight is small wrt. Z_0, that is $|\Delta Z| \ll Z_0$. The weak-perspective is thus the zero-order approximation of the full perspective projection (3). The error in image position is then $\mathbf{s}_{err} = \mathbf{s}_p - \mathbf{s}_{wp}$:

$$\mathbf{s}_{err} = -\frac{f}{Z_0}\frac{\Delta Z}{Z}\begin{bmatrix} X \\ Y \end{bmatrix} \tag{7}$$

showing that a small focal length (f), small field of view (X/Z_0 and Y/Z_0) and small depth variation ΔZ contribute to the validity of this model [5].

4.2 Linking Vision-Based Sensing to System Dynamics

The Vision-Based Model If we consider a fixed vision system observing a moving device $\mathbf{x}$, and assuming that only the device motion imply a sensor signal variation, the vision-based mapping could be written as follow:

$$\dot{\mathbf{s}} = \mathbf{J}_{\boldsymbol{\xi}}(\mathbf{s})\,\mathbf{v} \tag{8}$$

where $\dot{\mathbf{s}}$ is the observed feature motion vector in the image acquired from the digital microscope, and $\mathbf{v}$ is the device velocity screw in the Euclidean space. In our case the microrobot's velocity screw is reduced to its translational velocity, that is no angular motion is considered (cf. section 3.2), and $\mathbf{v} = (v_x, v_y, v_z)^T$. The term $\mathbf{J}_{\boldsymbol{\xi}}(\mathbf{s})$ is the Jacobian matrix, also referred as *image Jacobian* [17]. The subscript $\boldsymbol{\xi}$ denotes that $\mathbf{J}_{\boldsymbol{\xi}}(\mathbf{s})$ is a function of the extrinsic $\boldsymbol{\xi}_{\text{EX}}$ and intrinsic $\boldsymbol{\xi}_{\text{IN}}$ parameters of the sensor, and the tracked sensor features $\mathbf{s}$. The image Jacobian matrix could be decomposed as follow:

$$\mathbf{J}_{\boldsymbol{\xi}}(\mathbf{s}) = \mathbf{L}_{\boldsymbol{\xi}_{\text{IN}}}(Z, \mathbf{s})\mathbf{W}_{(\boldsymbol{\xi}_{\text{EX}})} \tag{9}$$

where $\mathbf{L}_{\boldsymbol{\xi}_{\text{IN}}}(Z, \mathbf{s})$ is referred as the *interaction matrix* [18], and the matrix $\mathbf{W}_{(\boldsymbol{\xi}_{\text{EX}})}$ allows to transform the velocity $\mathbf{v}$ between here the sensor frame $\mathcal{F}_c$ and the frame $\mathcal{F}_0$. As for

intrinsic parameters $\boldsymbol{\xi}_{\text{In}}$, the transformation matrix $\mathbf{W}_{(\boldsymbol{\xi}_{\text{Ex}})}$ is calibrated off-line [11,12]. In the case of a point $\mathbf{s} = (x, y)^T$, the interaction matrix could be easily derived from the full projection model (3), and for a translational motion is given by:

$$\mathbf{L}_{\boldsymbol{\xi}_{\text{In}}}(Z, \mathbf{s}) = \begin{pmatrix} -\frac{1}{Z} & 0 & \frac{x}{Z} \\ 0 & -\frac{1}{Z} & \frac{y}{Z} \end{pmatrix} \tag{10}$$

Using the weak-perspective, the above interaction matrix is then evaluated for the average plane Z_0.

Let us assume that the image Jacobian matrix $\mathbf{J}_{\boldsymbol{\xi}}$ is a full rank matrix, and then define $\mathbf{J}_{\boldsymbol{\xi}}^{+} = (\mathbf{J}_{\boldsymbol{\xi}}^T \mathbf{J}_{\boldsymbol{\xi}})^{-1} \mathbf{J}_{\boldsymbol{\xi}}^T$ its Moore-Penrose pseudo-inverse. Thus, the previous vision-based model equation (8) could be re-written as follow:

$$\mathbf{v} = \mathbf{J}_{\boldsymbol{\xi}}^{+} \dot{\mathbf{s}} \tag{11}$$

This relation allows to characterize the microrobot velocity in the 3D Euclidean space. Finally, let us notice that using this vision-based approach allows to estimate the 3D motion $\mathbf{v} = (v_x, v_y, v_z)^T$, which is not possible using the orthographic model and a single digital microscope.

Pushing the dynamics in the sensor-based model Now let us differentiate the vision-based model (8) to expose the sensor features dynamics:

$$\ddot{\mathbf{s}} = \mathbf{J}_{\boldsymbol{\xi}}(\mathbf{s})\, \dot{\mathbf{v}} + \mathbf{v} \cdot \mathbf{H}_{\boldsymbol{\xi}}(\mathbf{s}) \cdot \mathbf{v} \tag{12}$$

where $\mathbf{H}_{\boldsymbol{\xi}}(\mathbf{s})$ is the *image Hessian*, defined as:

$$\mathbf{H}_{\boldsymbol{\xi}}(\mathbf{s}) = \frac{\partial \mathbf{J}_{\boldsymbol{\xi}}(\mathbf{s})}{\partial \mathbf{s}} \mathbf{J}_{\boldsymbol{\xi}}(\mathbf{s}) = \mathbf{G} \mathbf{J}_{\boldsymbol{\xi}}(\mathbf{s}) \tag{13}$$

Substituting equation (11) into (12) yields:

$$\dot{\mathbf{v}} = \mathbf{J}_{\boldsymbol{\xi}}^{+} \left(\ddot{\mathbf{s}} - \mathbf{G}\, \dot{\mathbf{s}}\, \mathbf{J}_{\boldsymbol{\xi}}^{+}\, \dot{\mathbf{s}} \right) \tag{14}$$

This relation allows to characterize the microrobot acceleration $\dot{\mathbf{v}}$ in the 3D Euclidean space, using the image feature $\mathbf{s}$ provided by the digital microscope. Hence, using the force balance (2) the interaction force $\mathbf{f}_{\text{Ex}}$ could be estimated.

5 Experimental Validation

To calibrate the force $\mathbf{f}_{\text{Ex}}$ and validate the proposed approach, experiments within different environment have been conducted (see Fig. 6). Especially, each experiment is realized within static viscous fluid made of a mixture of water and 80% of glycerol ($\eta_f = 60\,\text{mPa/s}$). Furthermore, to facilitate the external force calibration a constant magnetic gradient is applied in the x-axis direction, and in the z-axis direction to compensate the gravitational force, leading to a straight line motion as depicted in Fig. 6.

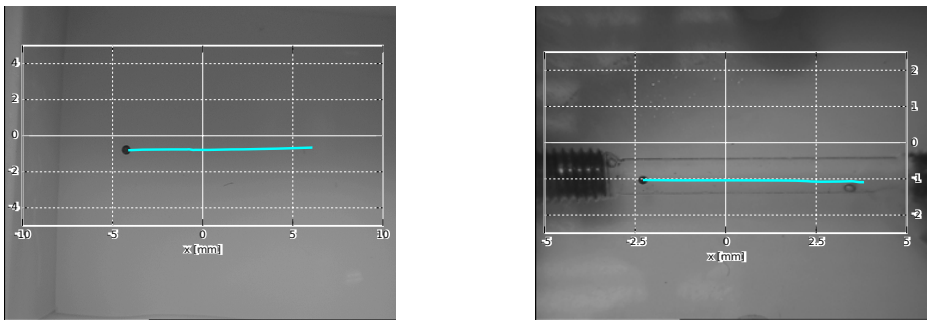

(a) (b)

Fig. 6. Experiments in (a) free extend and (b) in a channel of radius $R = 500\,\mu\mathrm{m}$.

5.1 Results in Free Extend

First, experiments in a viscous fluid with "no wall" are performed to calibrate the velocity and the interaction force without wall effects. Hence, van der Waals and electrostatic forces could be effectively neglected, and mainly the hydrodynamic and the gravitational forces could be considered in the interaction force expression (2). Within this free extend the average depth of the weak-perspective is calibrated at $Z_0 = 67.67\,\mathrm{mm}$. Fig. 7 shows the velocity and acceleration error norm between the orthographic projection and the weak-perspective models. A velocity error of an average $0.9931\,\mathrm{m/s}$, and an acceleration error of $2.6328\,\mathrm{m/s^2}$ is noticed, for an overall mean velocity of $2.4758\,\mathrm{m/s}$. As the orthographic projection model is less reliable, it tends to underestimate the velocity, implying a poor acceleration estimation.

Thus, knowing the microrobot motion in the free extend, the system's dynamic model introduced in Sect. 3.2 is used. Fig. 8(a) shows the computed forces using the orthographic perspective whereas Fig. 8(b) with weak-perspective models. As the orthographic model is mainly based on the 2D vision data, only the hydrodynamic drag force could be considered. Indeed, using such projective model only 2D motion could be retrieved. Especially, by neglecting the depth information, the orthographic projection models image formation incorrectly and misestimates the unknowns parameters. In contrast, our proposed framework based on the weak-projection allows us to consider the full 3D motion and system's dynamics. Therefore, thanks to our proposed approach we are able to consider the gravitational forces $\mathbf{f}_g$, and improve the force balance model (2). In particular, Fig. 9 presents the difference between the logarithmic error between the force balance model (2) and the microrobots acceleration computed from vision-based measurements. As one can see, our framework seems to validate the proposed system's dynamic model.

5.2 Results within a MicroChannel

Secondly, experiments in a viscous fluid within a channel of radius $R = 500\,\mu\mathrm{m}$ are realized. The average depth is here calibrated at $Z_0 = 85.26\,\mathrm{mm}$, and the distance to the

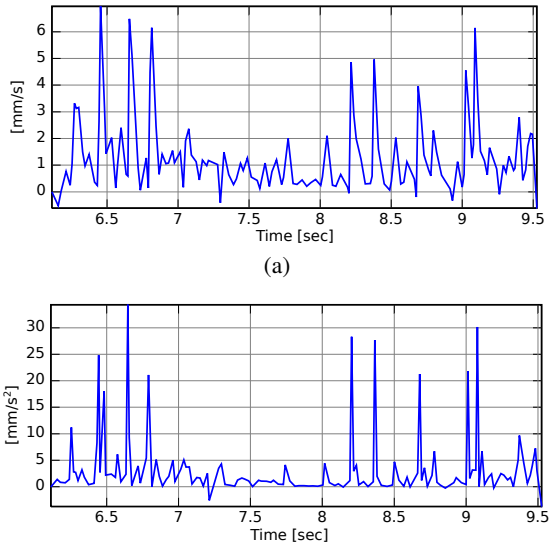

Fig. 7. Error norm between the orthographic perspective and the weak-perspective: (a) velocity $\mathbf{v}$ and (b) acceleration $\dot{\mathbf{v}}$.

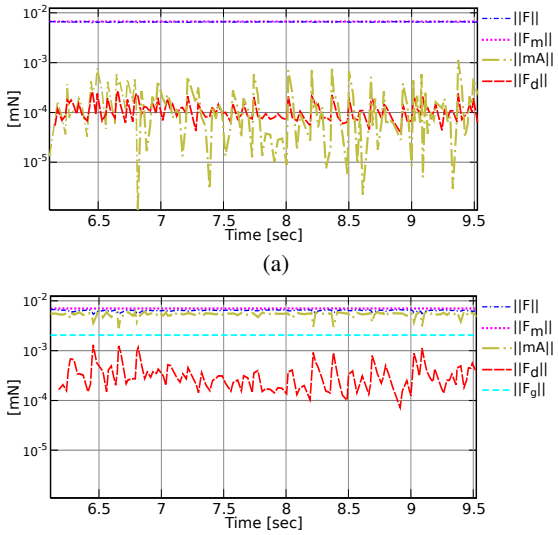

Fig. 8. Forces model and magnetic microrobot's dynamic using (a) the orthographic perspective and (b) the weak-perspective models.

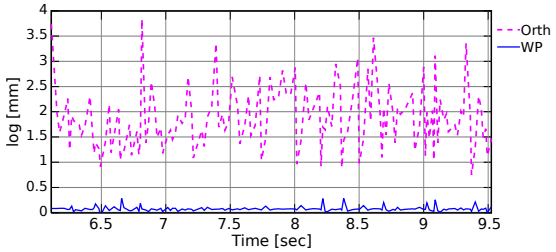

Fig. 9. Comparison between the force balance model and the microrobot dynamics in a free extend: $\log \|F\| - \log \|m\dot{\mathbf{v}}\|$.

wall is in average of $\delta = 0.256\,\mathrm{mm}$. In such microfluidic environment, van der Waals forces remain negligible (as it was in the order of 10^{-14} mN) whereas the electrostatic forces become significant, as illustrated on Fig. 10. Fig. 11 shows the logarithmic error between the force balance model (2) and the microrobots acceleration computed using our proposed approach based on the weak-perspective model. In particular the dashed line represents the logarithmic error when no electrostatic forces is considered, in contrast to the solid line. As one can see, adding the electrostatic forces knowledge may help to improve the system's dynamic model.

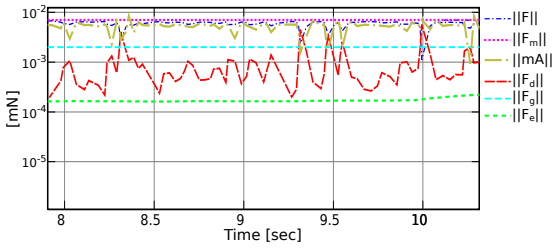

Fig. 10. Forces model and magnetic microrobot's dynamic in a microchannel.

6 Conclusions

In this paper calibration and validation of a magnetic microrobot that navigate in viscous fluid is presented. First the controlled magnetic forces exerted on the magnetic microrobot is calibrated, and the obtained results validate the magnetic model. Secondly, the external forces are characterized on-line from the image acquired from a digital microscope. To this aim a mapping between the vision-based data and the system's dynamic model is expressed. More precisely, unlike classical approach that uses an orthographic projection model when a microscope is considered, we have proposed here to deal with the weak-perspective model. Indeed the weak-perspective is known to be closer to the full perspective. Moreover, the proposed vision-based formalism allows to retrieve the

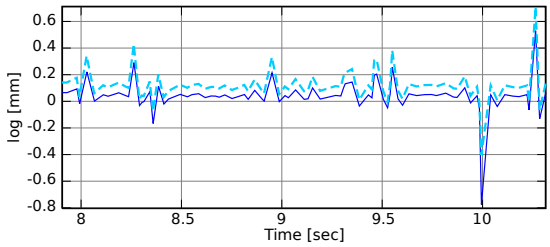

Fig. 11. Comparison between the force balance model and the microrobot dynamics in a microchannel: $\log \|F\| - \log \|m\dot{\mathbf{v}}\|$. Dashed-line without electrostatic forces, solid line with electrostatic forces.

3D motion and dynamic, and help us to characterize the external force. Furthermore, the experimental results illustrate the efficiency of the proposed framework, and validate the system's dynamic model. Future extends will consider other experiments with varying microball and microchannel sizes.

References

1. Abbott, J., Nagy, Z., Beyeler, F., Nelson, B.: Robotics in the Small. IEEE Robot. Automat. Mag. (2007) 92
2. Nelson, B.J., Kaliakatsos, I.K., Abbott, J.J.: Microrobots for minimally invasive medicine. Annual Review of Bio.med. Eng. **12**(1) (2010) 55–85
3. Abbott, J.J., Peyer, K.E., Lagomarsino, M.C., Zhang, L., Dong, L.X., Kaliakatsos, I.K., Nelson, B.J.: How should microrobots swim? Int. J. of Robot. Res. (July 2009)
4. Martel, S., Mathieu, J.B., Felfoul, O., Chanu, A., Aboussouan, E., Tamaz, S., Pouponneau, P., Yahia, L., Beaudoin, G., Soulez, G., Mankiewicz, M.: Automatic navigation of an untethered device in the artery of a living animal using a conventional clinical magnetic resonance imaging system. Applied Physics Letters **90**(11) (2007) 114105
5. Xu, G., Zhang, Z.: Epipolar geometry in stereo, motion and object recognition: a unified approach. Volume 6. Springer (1996)
6. Clime, L., Le Drogoff, B., Zhao, S., Zhang, Z.: Magnetic nanocarriers: from material design to magnetic manipulation. Int. J. of Nanotechnology **5**(9) (2008) 1268–1305
7. Arcèse, L., Fruchard, M., Beyeler, F., Ferreira, A., Nelson, B.J.: Adaptive backstepping and mems force sensor for an mri-guided microrobot in the vasculature. In: IEEE Int. Conf. on Intel. Robot. and Automation, Shanghai, China (May 2011)
8. Yesin, K., Vollmers, K., Nelson, B.: Modeling and control of untethered biomicrorobots in a fluidic environment using electromagnetic fields. Int. J. of Robot. Res. **25**(5-6) (2006) 527–536
9. Belharet, K., Folio, D., Ferreira, A.: Control of a magnetic microrobot navigating in microfluidic arterial bifurcations through pulsatile and viscous flow. In: IEEE/RSJ Int. Conf. on Intel. Robots and Systems (IROS?2012), Vilamoura, Algarve, Portugal (October 2012) 2559–2564
10. Arcèse, L., Fruchard, M., Ferreira, A.: Endovascular Magnetically-Guided Robots: Navigation Modeling and Optimization. IEEE Trans. Biomed. Eng. **59**(4) (2012) 977–987
11. Tsai, R.: A versatile camera calibration technique for high-accuracy 3D machine vision metrology using off-the-shelf tv cameras and lenses. IEEE J. Robot. Automat. **3**(4) (August 1987) 323–344

12. Bouguet, J.Y.: Camera calibration toolbox for matlab (2004)
13. Oliensis, J.: A critique of structure-from-motion algorithms. Comp. Vis. and Image Understanding **80**(2) (2000) 172–214
14. Matthies, L., Kanade, T., Szeliski, R.: Kalman filter-based algorithms for estimating depth in image sequences. Int. J. of Computer Vision **3**(3) (1989) 209–238
15. Thrun, S., Fox, D., Burgard, W., Dallaert, F.: Robust mote-carlo localization for mobile robots. Artifial Intelligence **128**(1-2) (May 2001) 99–141
16. Folio, D., Cadenat, V.: Dealing with visual features loss during a vision-based task for a mobile robot. Int. J. of Optomechatronics **2** (2008) 185–204
17. Hutchinson, S., Hager, G., Corke, P.: A tutorial on visual servo control. IEEE Trans. Robot. Automat. **12**(5) (October 1996) 651–670
18. Chaumette, F., Hutchinson, S.: Visual servo control, part I: Basic approaches. IEEE Robot. Automat. Mag. **13**(4) (December 2006) 82–90